Geomechanics and Engineering, *Vol. 35, No. 4 (2023) 411-424*
https://doi.org/10.12989/gae.2023.35.4.411

A modified shell-joint model for segmental tunnel dislocations under differential settlement

Jianguo Liu[1,2a], Xiaohui Zhang*[1,2], Yuyin Jin[1,2b] and Wenyuan Wang[1,2c]

[1]*Key Laboratory of Road and Traffic Engineering of the Ministry of Education, Tongji University, Shanghai 201804, China*
[2]*Shanghai Key Laboratory of Rail Infrastructure Durability and System Safety, Tongji University, Shanghai 201804, China*

(*Received June 26, 2021, Revised April 3, 2023, Accepted November 2, 2023*)

Abstract. Reasonable estimates of tunnel lining dislocations in the operation stage, especially under longitudinal differential settlement, are important for the design of waterproof gaskets. In this paper, a modified shell-joint model is proposed to calculate shield tunnel dislocations under longitudinal differential settlement, with the ability to consider the nonlinear shear stiffness of the joint. In the case of shell elements in the model, an elastoplastic damage constitutive model was adopted to describe the nonlinear stress-strain relationship of concrete. After verifying its applicability and correctness against a full-scale tunnel test and a joint shear test, the proposed model was used to analyze the dislocation behaviors of a shield tunnel in Shanghai Metro Line 2 under longitudinal differential settlement. Based on the results, when the tunnel structure is solely subjected to water-earth load, circumferential and longitudinal joint dislocations are all less than 0.1 mm. When the tunnel suffers longitudinal differential settlement and the curvature radius of the differential settlement is less than 300 m, although maximum longitudinal joint dislocation is still less than 0.1 mm, the maximum circumferential joint dislocation is approximately 10.3 mm, which leads to leakage and damage of the tunnel structure. However, with concavo-convex tenons applied to circumferential joints, the maximum dislocation value reduces to 4.5 mm.

Keywords: dislocation; longitudinal differential settlement; modified shell-joint model; segmental tunnel lining

1. Introduction

Shield tunnel linings are composed of prefabricated concrete segments and joints, in which the joint sections are the weaker parts of the structures owing to their lower stiffness than the main segment sections (Zhang *et al.* 2023b). Engineering experiences show that dislocations between adjacent segments of the joint are common in shield tunnels, especially when longitudinal differential settlement occurs, including dislocations in the circumferential and longitudinal joints (see Fig. 1). Dislocations in the operation stage reduce the contact area between the gaskets that are installed in the joint section to prevent water leakage, thus influencing the waterproof capability of the tunnel (Zhang *et al.* 2023a, Zhang *et al.* 2019, Shi *et al.* 2019, Zou *et al.* 2017). An experimental test on the waterproof capability of the gaskets in the tunnel joint conducted by Zhang *et al.* (2020) shows that the ultimate water pressure for leakage decreases from 1.2 MPa to 0.6 MPa when the dislocation value increases from 2 mm to 10 mm. Therefore, it is of great significance to ascertain the dislocations of the tunnel joint in the operation stage to guide the optimal design of the waterproof gasket.

Many scholars have proposed analytical models to study the mechanical behavior of segmental tunnel joints. Considering the tunnel lining a half-infinite beam on an elastic foundation, Talmon and Bezuijen (2013) analyzed the relationship between the joint deformation and bending moment. Tvede-Jensen *et al.* (2017) proposed an analytical approach to determine the joint's nonlinear bending moment–rotation relations through a mechanical analysis of the joint. Using similar methods, Zhang *et al.* (2019b) studied the relationship between the height of the concrete compression zone and the rotation angle of the joint under different compression-bending combinations. Using the Euler beam-spring model, Wang *et al.* (2020) studied the internal forces of the tunnel lining under different soil pressures, and the joint in his model was simulated by a set of linear springs with shearing, compression, and rotation forces. In the case where the shear stiffness of the joint is related to the axial force, Li *et al.* (2019) and Yang *et al.* (2019) adopted a contact friction model to analyze the relationship between the dislocation and shear force. However, when the dislocation reaches a certain large value, the bolts in the joint may yield, implying that the relationship is much more complex and nonlinear than that described in the contact friction model.

To observe the actual failure process and characteristics of the tunnel joint, some scholars conducted joint tests and whole ring tests of a segmental tunnel with complex engineering geological conditions.With the designed joint bending tests for different axle forces, Jin *et al.* (2017) and Zuo *et al.* (2018) obtained the relationship between the opening of the joint and the bending motion. Feng *et al.*

---

*Corresponding author, Associate Professor
E-mail: 1988xiaohui@tongji.edu.cn
[a]Ph.D.
[b]Ph.D. Student
[c]MA.Sc

http://www.techno-press.org/?journal=gae&subpage=7
ISSN: 2005-307X (Print), 2092-6219 (Online)

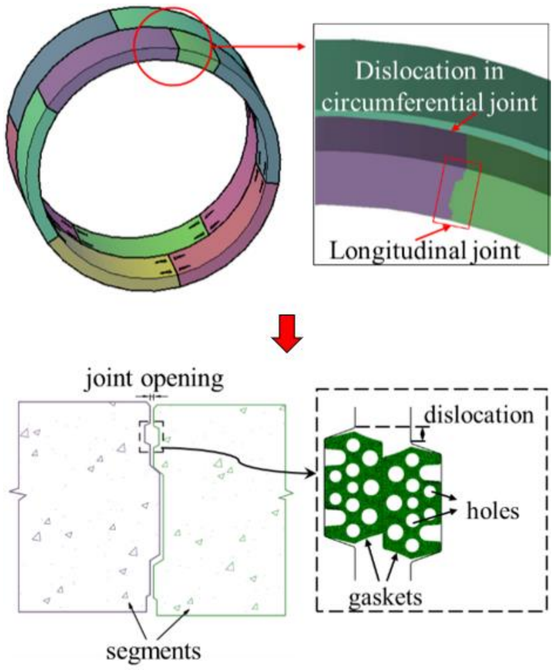

Fig. 1 Sketch of shield tunnel dislocations

(2018) performed a full-scale experiment to study the bending stiffness of a joint under different combinations of compression values and bending moments. Salemi et al. (2015) conducted experimental direct shear tests on concrete samples of contact points in segments and developed a precise contact model for the normal and shear resistance of segmental tunnel linings to obtain the shear stiffness of the joint. Ding *et al.* (2020) conducted a series of full-scale mechanical loading tests on the joint with combined axis force, moment, and shear force. The effect of the shear force on the mechanical capacity, deformation, and duality of the segment joint was investigated by Ding *et al.*

Owing to the enormous cost of experimental tests and the assumptions of simplified models, some scholars have adopted three-dimensional (3D) finite element (FE) models to study the mechanical behavior of the tunnel structure (Nawel and Salah 2015, Eskandari *et al*. 2018, Do *et al.* 2014, Nikadat and Marji 2016). Using a 3D FE model of the tunnel and joints, Shi *et al.* (2016) studied the mechanical and deformation characteristics of a tunnel under the effect of a nearby excavation. To further improve the calculation efficiency of the 3D FE model, the segment was simplified as a shell, and the joint structure was simulated by springs (Li *et al*. 2014). Hasan *et al.* (2019) used a pseudoshell model to investigate the effect of static loads and pseudoshell thickness on the crack opening and propagation of tunnel structures. The stiffness of the springs was a significant parameter for the mechanical analysis of the tunnel; therefore, detailed 3D FE models were used to describe the relationship between the bending and shear stiffness with internal forces (Yan *et al*. 2019, Shi *et al*. 2016, Wang *et al*. 2012, Salemi *et al*. 2015). Furthermore, the stiffness was assumed to be a constant, tri-linear function, or other nonlinear functions (Chen *et al.* 2018, Wang *et al*. 2019).However, the coupling relationship between the shear stiffness, axial force, and dislocation was not considered in the shell-spring model.

In this study, a modified shell-joint model analyzes the dislocations of the shield tunnel during the operation stage, in which the configuration of the joint is considered. The proposed model is verified through comparison with a whole ring test for the mechanical behavior of the tunnel. The modified shell-joint model was then used to study the dislocation of the shied tunnel in the Shanghai Metro under the longitudinal differential settlement. The effects of the concavo-convex tenon on controlling dislocation development were also analyzed.

2. Modified shell-joint model of the segmental tunnel lining

Shell-joint models can systematically consider the conformation discontinuities of the longitudinal and circumferential joints of the tunnel, enabling the analysis of the dislocation behavior of the segmental joint. The traditional shell-joint model is modified in this study to consider the nonlinear shear stiffness of the joint using a user-defined link element. The parameters of the nonlinear shear stiffness in the link element are obtained using a 3D FE model and are assumed to be a function of both the axial force at the joints and the joint dislocation value.

2.1 Outline of the shell-joint model

As shown in Fig. 2, the concrete segments of the tunnel are modeled by three-dimensional shell elements, and the joint configurations are simulated by discretized link elements that are assigned with a certain stiffness obtained from the three-dimensional model to simulate the link between adjacent segments and rings. The model is established by the secondary development of an FE software, and the stiffness of the link elements is expressed in cylindrical coordinates. Simultaneously, the model is subjected to displacement constraint at one end and uniformly distributed load at the other end to simulate the thrust of the jack as boundary conditions. Axis t, r, and z in Fig. 2 represent the tangential, radial, and longitudinal directions of the cross-section of the shield tunnel, respectively.

2.1.1 Shell elements of the tunnel lining

The shell element in the model comprises a concrete layer and steel bar layer with a unified displacement function to consider their contributions to the element stiffness matrix K_c^e. Specifically, K_c^e can be obtained based on the superposition of each layer's contribution, described by Eq. (1)

$$K^e = K_c^e + K_s^e \tag{1}$$

where K_c^e and K_s^e are the contributions of the concrete layer and steel bar layer to the element stiffness matrix, respectively. The elastoplastic damage constitutive model was adopted to describe the stress-strain relationship of

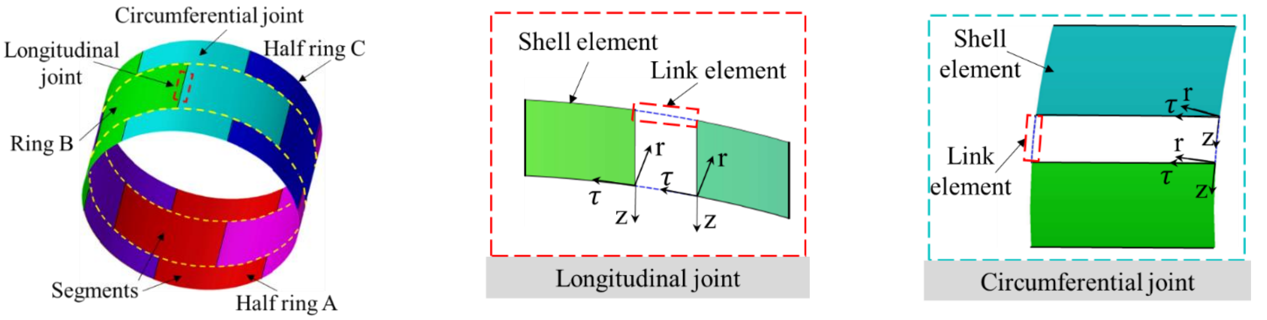

(a) Outline of the model (b) Details of the longitudinal joint (c) Details of the circumferential joint

Fig. 2 Modified shell-joint model of the tunnel

(a) Stiffness of the longitudinal joint (b) Stiffness of the circumferential joint

Fig. 3 Joint stiffness levels in different directions

concrete. Parameters including the tensile damage factor d_t and compression damage factor d_c, which can be determined according to specifications in GB 50010-2010 (2010), describe the different damage characteristics of the concrete under tension and compression conditions, as shown in Eqs. (2) and (3)

$$\sigma_t = (1-d_t)E_0(\varepsilon_t - \tilde{\varepsilon}_t^{pl}) \tag{2}$$

$$\sigma_c = (1-d_c)E_0(\varepsilon_c - \tilde{\varepsilon}_c^{pl}) \tag{3}$$

where $\tilde{\varepsilon}_t^{pl}$ and $\tilde{\varepsilon}_c^{pl}$ are the tensile and compression equivalent plastic strains, respectively; E_0 is the initial elastic modulus; σ_t and σ_c are the tensile and compressive stresses, respectively.

A classical double line model was adopted when assigning the properties of steel bars. Based on the HPB300 steel bar, which is widely used in shield tunnel segments, the yield strength of the steel bar in the model was 300 MPa, and the ultimate tensile strength was 420 MPa.

2.1.2 Link elements of the joint

The link element of the segmental joint is proposed in this section to express the relationship between the internal force and deformation of the joint as follows

$$\{\Delta F\}=[K]\{\Delta d\} \tag{4}$$

where $[K]$ is the stiffness matrix of the link element, $\{\Delta d\}$ and $\{\Delta F\}$ are the relative displacement and force, respectively, of the link element between nodes i and j, and they are expressed as Eq. (5). where r_k, t_k, z_k, θ_{rk}, θ_{tk}, and θ_{zk} are the generalized displacements of node k ($k = i$ or j) in and around *the r*, *t*, *and z* directions, respectively; F_{rk}, F_{tk}, F_{tk}, M_{rk}, M_{tk} and M_{zk} are the generalized force components of node k ($k = i$ or j) in and around *the r*, *t*, *and z* directions, respectively.

The stiffness matrix $[K]$ of the link element is a diagonal matrix composed of six stiffness elements. As shown in Fig. 3, for the longitudinal joints, Kr, Kt, and Kz correspond to the translational stiffness in r, t, and z directions, whereas Kθr, Kθt, and Kθz correspond to the rotational stiffness in r, t, and z directions, respectively. It should be noted that the longitudinal joint stiffness matrix and circumferential joint stiffness matrix are determined based on the same assumption as follows (taking the link element of the longitudinal joint as an example):

(a) K_t (tensile or compression stiffness): It is assumed that the compression stiffness of the link element at the bolt's position is set based on the compression stiffness of concrete, whereas the tensile stiffness is set based on the tensile stiffness of the bolt. Link elements at positions without components such as bolts are considered to only be able to withstand the compression force, such that the tensile stiffness is set to 0.

(b) K_r (radial shear stiffness): To consider the convex tenon), the shear stiffness of the link element is

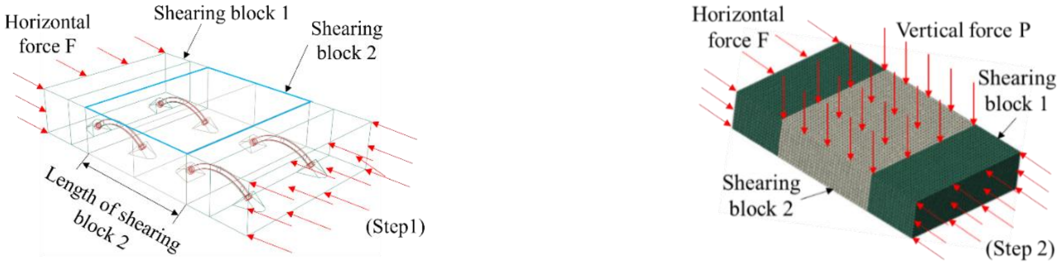

(a) Horizontal force F in step 1 (b) Vertical force P in step 2

Fig. 4 Forces applied on the concrete blocks in the FE model

$$\{\Delta F\}=\{F_{ri}-F_{rj} \quad F_{ti}-F_{tj} \quad F_{zi}-F_{zj} \quad M_{ri}-M_{rj} \quad M_{ti}-M_{tj} \quad M_{zi}-M_{zj}\}^T \tag{5}$$

$$\{\Delta d\}=\{r_i-r_j \quad t_i-t_j \quad z_i-z_j \quad \theta_{ri}-\theta_{rj} \quad \theta_{ti}-\theta_{tj} \quad \theta_{zi}-\theta_{zj}\}^T \tag{6}$$

obtained by a 3D FE model, which can be described by a complex function of the axial force, shear force, and dislocation.

(c) K_z (longitudinal shear stiffness): The longitudinal stiffness of the link element can also be obtained using a 3D FE model as the radial shear stiffness.

(d) $K_{\theta t}$ (tangential torsional stiffness): The tangential torsion of the joint generates the radial shear force between segments, and the corresponding torsion value is affected by the shear stiffness of the link element. Thus, the capacity of the joint against tangential torsion can be described by the link elements with a radial shear stiffness; therefore, the tangential torsional stiffness is set as 0.

(e) $K_{\theta z}$ (circumferential bending stiffness): The bending stiffness of the link element is determined based on the nonlinear relationship between the bending moment and rotation angle of the tunnel joint.

(f) $K_{\theta r}$ (radial bending stiffness): Because the radial bending moment can be described as the tensile and compression forces on several adjacent link elements, the joint's capacity to withstand the radial bending moment can be represented by the tension and compression stiffness of the link element. Thus, the radial bending stiffness of the link element was set as 0.

2.2 Three-dimensional finite element approach to obtain joint shear stiffness

A 3D FE analysis was conducted to obtain the radial and longitudinal shear stiffnesses of the joint, as shown in Fig. 4. The FE model comprises one whole shearing block (block 2 in Fig. 4), two adjacent half blocks (block 1 in Fig. 4), and bolts between shearing blocks. Both concrete blocks and bolts were modeled using continuum 3D 10-node (C3D10) solid elements.

The elastoplastic damage constitutive model was adopted to describe the stress-strain relationship of the concrete, whereas the double line model was used as the constitutive model of the bolt. All normal contacts in the model, including contacts between adjacent segments, were set as hard contacts. The tangential behavior between segments was set through the penalty method. Penalty method is a way to determine frictional forces between two contacted segments under dislocation. A coefficient will be assigned to calculate the frictional force combined with the normal contact force. In the 3D model, the tangential behaviors between of the two adjacent segments in the concrete region were simulated as penalty method to further determine the shear stiffness of the joints.

In the case of the circumferential and longitudinal joints with bolts, the preload force of the bolts was applied to the model during simulation, as shown in Eq. (7)

$$F_s=C_s\sigma_s A_s \tag{7}$$

where σ_s and A_s are the yield strength and the cross-sectional area of the bolt, respectively; C_s is the safety coefficient of the bolt preload force, which is assumed as 0.5, in this study.

As illustrated in Fig. 4(a), the horizontal force F is applied to the cross-sections at the two ends of the blocks in the load-controlled mode to simulate the compression or tensile force between adjacent segments or lining rings in step 1. In step 2, the vertical force P is applied to the top of shearing block 2 in the displacement-controlled mode to simulate the shear process of the joint. It should be noted that the vertical force P should be replaced by the longitudinal force when determining the longitudinal shear stiffness of the joint. Subsequently, the relationship between the shear force and dislocation at the joint under certain axial forces can be obtained.

To analyze the mechanical behavior of the joint when subjected to shear force, a 3D FE model was used to simulate the shear process of a longitudinal joint with two M33 straight bolts. The diameter of bolt holes is designed based on actual conditions, as shown in Fig. 5(a). The parameters of the FE model are listed in Table 1, where the width and thickness of shearing block 2 were designed

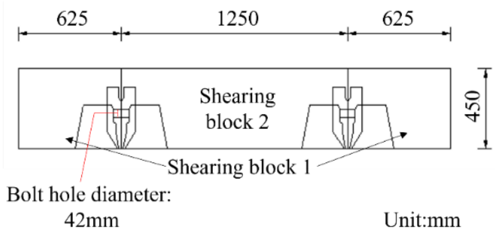

(a) Dimensions of shear block and bolt hole

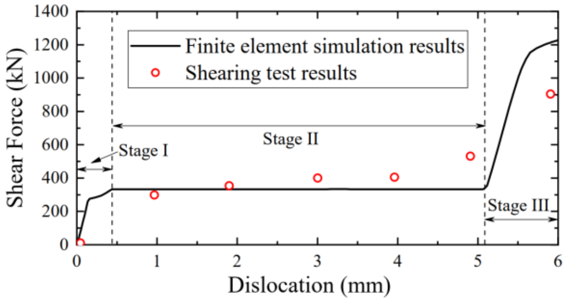

(b) Shear Force-Dislocation curves from FE simulations and the shearing test

Fig. 5 Results of FE simulations and shearing test

Table 1 Parameters of the FE model

Concrete grade	Bolt grade	Dimensions of shearing block 2		
		Length	Width	Thickness
C50	M33	1250 mm	1200 mm	450 mm

based on the actual segments used in the shield tunnels in Shanghai. The length of the shear block 2 is determined based on commonly used joint shear tests. The shear force-dislocation curve calculated by the FE model was compared to that from a joint shear test by Liu *et al.* (2016), as shown in Fig. 5(b). It can be observed from the figure that the trend of the calculated shear force – dislocation curve coincides with the experimental result. Both the calculated and measured data show a three-stage characteristic of the shear process, as follows:

Stage I (friction shearing stage): When the shear force is smaller than the static frictional force on the joint surface, there is virtually no relative displacement between the bolt and the hole.

Stage II: Obvious dislocation starts occurring between adjacent shearing blocks when the shear force exceeds the static frictional force.However, the two ends of the bolt made no contact with the holes.

Stage III: The two ends of the bolt contact the holes of the adjacent shearing blocks, and the stress concentration starts appearing in the middle of the bolt.

3. Verification of the modified shell-joint model

The proposed modified shell-joint model was verified against a full-ring experiment for the Shanghai Yangtze River tunnel and the corresponding 3D FE simulations (Wang 2007). The shield tunnel is staggered-fabricated with 10 lining blocks per segmental ring, with an inner diameter of 13.7 m and an outer diameter of 15 m. The width of a single segmental ring is 2 m. Each longitudinal joint adopts two M39 oblique bolts with a spacing of 1 m, and the circumferential joint adopted 38 M30 bolts. In the full-ring experiment, a whole ring and its two adjacent half rings were chosen for testing with 44 concentrated forces applied, as shown in Fig. 6.

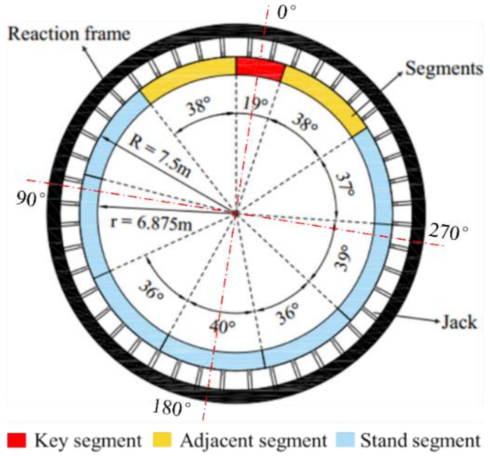

Fig. 6 Sketch of the full-scaled experiment

Table 2 Compression and tensile stiffness of the link element

Concrete grade	Spacing between link elements (mm)	Elastic modulus of concrete (N/mm^2)	Length of link elements (mm)	Compression stiffness (N/mm)
C50	100	3.45E+04	10	2.24E+08
Bolt Grade	Diameter of bolts (mm)	Elastic modulus of bolts (N/mm^2)	Length of link elements (mm)	Tensile stiffness (N/mm)
M30	30	2.10E+05	10	1.48E+07
M36	39	2.10E+05	10	2.51E+07

In the proposed modified shell-joint model, the bending and shear stiffness matrix of the link element are based on the experiments of Chen *et al.* (2010) and Li *et al.* (2011) for the same tunnel structures. The compression and tensile stiffness values of the link elements are listed in Table 2, where the length of the link element is determined as 10 mm, based on the clearance control of shield tunnels in the Shanghai, China.

The bending moment and radial displacement of the segmental ring and radial dislocation of the circumferential joint were calculated using the proposed shell joint model and compared with those obtained from the full-scale experiment and the 3D FE simulation, with the results illustrated in Fig. 7. It can be observed from the figure that the maximum positive bending moment, which is approximately 600 kN·m, appears at the top and bottom of the tunnel, whereas the negative bending moment appears at

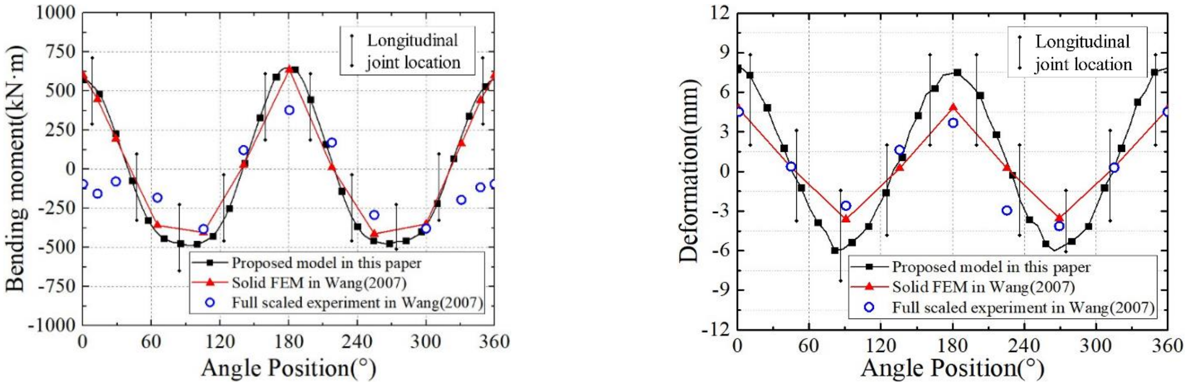

(a) Bending moment of the tunnel ring (b) Radial displacement of the tunnel ring

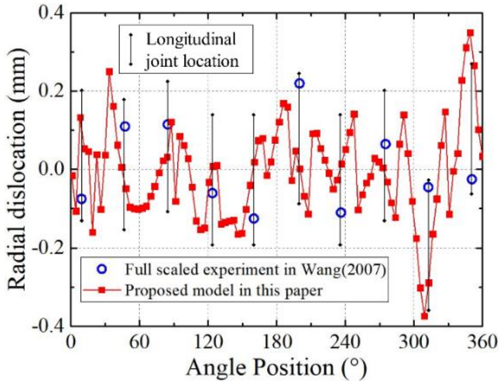

(c) Radial dislocation of the circumferential joint

Fig. 7 Comparison between measured data and simulation results

the arch waist. Under the effect of this bending moment, the segments at the top and bottom of the tunnel move inward, as shown in Fig. 7(b), and the segments at the arch waist move outward, making the tunnel ring a horizontal ellipse shape. However, the radial dislocations of the circumferential joints in Fig. 7 (c) are all less than 0.4 mm because the loads applied on the tunnel rings are consistent in the longitudinal direction.

While the proposed model and the solid FEM model showed minimal differences in the bending moment, notable discrepancies can be observed when compared to experimental results at 0-30° and 330-360° of the tunnel. It can be explained that the bending moments of the lining segment in Wang's experiment are approximated based on concrete strain and steel bar stress measurement results. Due to the complex structure assembly and multiple interfaces around the key segment, installation space for measurement devices is limited, potentially resulting in significant testing errors at this location. In summary, the figure demonstrates a good agreement between the bending moment, radial displacement, and dislocations obtained by the modified shell-joint model and the full-scale experiment in the majority of tunnel positions, implying the applicability of the modified shell-joint model.

4. Effect of the longitudinal differential settlement on dislocations of the tunnel

4.1 Joint dislocation under the longitudinal differential settlement

In the operation stage, many factors can affect the displacement and deformation of the tunnel structure (Yoo *et al*. 2020, Wang *et al*. 2010, Zaid 2021). Among these factors, longitudinal differential settlement is frequently encountered and has a significant effect on joint dislocations during the operation stage (Gong *et al*. 2015, Kim *et al*. 2020). However, the traditional longitudinal structural model simplifies the tunnel as an Euler-Bernoulli beam and ignores the dislocations between adjacent tunnel rings (Wu *et al*. 2018). In this section, the modified shell-joint model is used in studying the joint dislocation behaviors of a circular shield tunnel in Shanghai Metro Line 2 when longitudinal differential settlement occurs (see Fig. 8).

The shield tunnel comprises six lining blocks per segmental ring, with an inner diameter of 5.5 m and an outer diameter of 6.2 m. The width of a single segmental ring is 1.2 m. Adjacent segmental rings are connected by bolts with a diameter of 30 mm. As illustrated in Fig. 9, an 11-ring lining model was established using FE software, adopting a three-dimensional shell element with an elastoplastic damage constitutive model to simulate the concrete segments. The parts used in the three-dimensional model to obtain the shear stiffness of the joints are shown in Fig. 10.

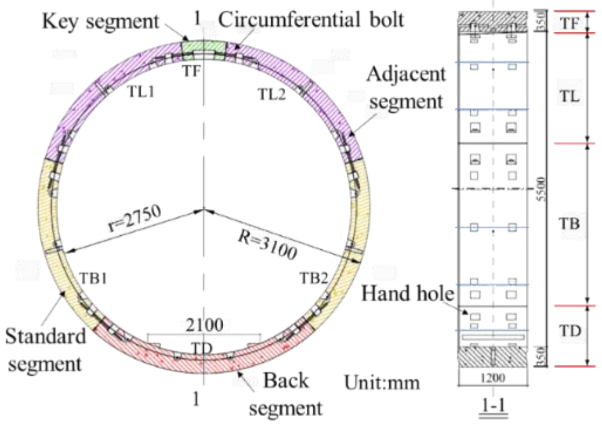

Fig. 8 Cross-section and details of the shield tunnel in Shanghai Metro Line 2

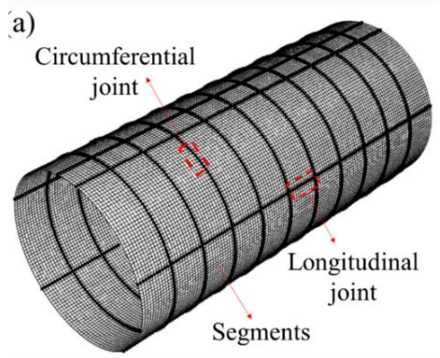

(a) Isometric view of the 11-ring model

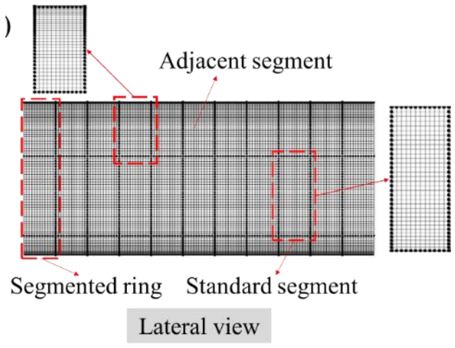

(b) Lateral view of the 11-ring model

Fig. 9 Finite element model for the eleven segmental rings

The shear stiffness function of the link element was obtained using a solid FE model, as shown in Fig. 11(a). The bending stiffness function of the link element in Fig. 11(b) adopts the trilinear elastoplastic bending moment-rotation angle curve, which is referred to in a study by Liu *et al*. (2016) on the flexural capacity of the tunnel joint. The compression and tensile stiffness values of the link elements are listed in Table 2.

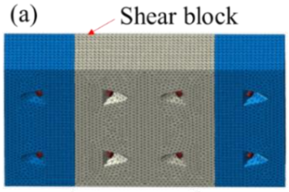

(a) Schematic of the three-dimensional model

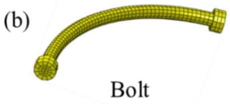

(b) Bolt in the three-dimensional model

(c) Half shear block in the three-dimensional model

(d) Shear block in the three-dimensional model

Fig. 10 Three-dimensional model for obtaining the shear stiffness of the joint without the concavo-convex tenon

Table 3 Displacements at the arch waist under longitudinal differential settlements

Curve radius(m)	Deflections at arch waist (mm)					
	Ring 1, 11	Ring 2, 10	Ring 3, 9	Ring 4, 8	Ring 5, 7	Ring 6
300	0.00	21.60	38.40	50.40	57.61	60.01
500	0.00	12.96	23.04	30.24	34.56	36.00
1000	0.00	6.48	11.52	15.12	17.28	18.00
2000	0.00	3.24	5.76	7.56	8.64	9.00
3000	0.00	2.16	3.84	5.04	5.76	6.00
5000	0.00	1.30	2.30	3.02	3.46	3.60
10000	0.00	0.65	1.15	1.51	1.73	1.80
15000	0.00	0.43	0.77	1.01	1.15	1.20

Soil loads corresponding to a buried depth of 20 m were applied to the tunnel to achieve an accurate initial state before applying a longitudinal differential settlement. Based on the research by Wu *et al*. (2015), there exist a longitudinal shear transfer effect and circumferential flattening effect when a tunnel's longitudinal deformation occurs. To avoid the influence of unreasonable loading mode on the flattening effect, a mandatory displacement was applied to the arch waist of each segment ring to simulate the longitudinal differential settlement of the shield tunnel, as shown in Fig. 12.

The longitudinal cumulative settlement curve can be fitted based on the measured tunnel data. The curve radius

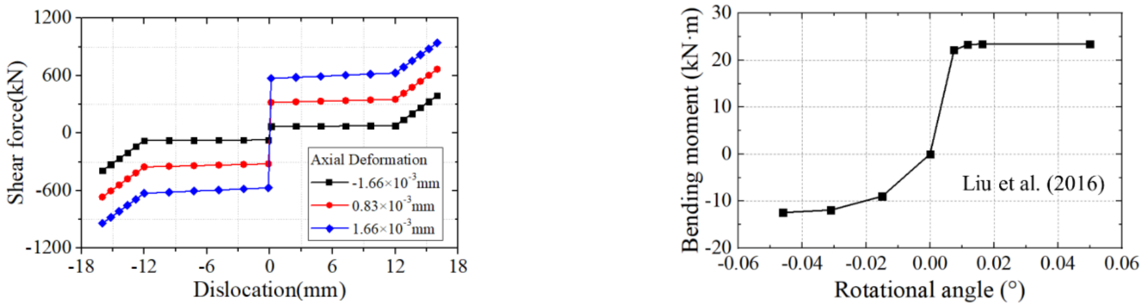

(a) Shear stiffness function

(b) Bending stiffness function

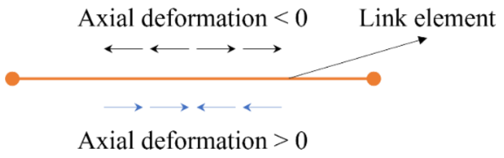

(c) Deformation direction of link element

Fig. 11 Stiffness function of the link element

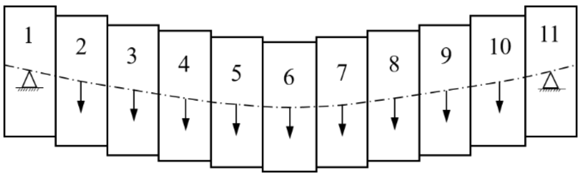

Fig. 12 Longitudinal differential settlement applied on the tunnel linings

in this section is set from 300 m to 15000 m, and the corresponding mandatory displacements are applied to the arch waist of the segment rings, as listed in Table 3.

The dislocations in the longitudinal and circumferential joints subjected solely to the soil load are shown in Fig. 13. It can be observed from the figure that the maximum dislocations in different circumferential joints are all less than 0.24 × 10-3 mm, which can be explained by the fact that the soil pressure is evenly distributed on the 11 rings. The maximum circumferential dislocation appears at 335° and 25°, which is around the position of the longitudinal bolt in the adjacent segment. However, dislocations of the circumferential joint between different lining rings differ from each other, and the largest one appears at the circumferential joint between rings 5 and 6.

In the case of the dislocation of the longitudinal joint in a lining ring, the maximum value is less than 0.21 × 10-3 mm. In a segmental ring, the dislocations at the longitudinal joints between the standard segment and adjacent segment (i.e., joints at TL1-TB1 and TL2-TB2) are approximately six times those at the other longitudinal joints. Under the condition of bearing only soil loads, the maximum deformation of the lining ring occurs at the waist, while the joints at TL1-TB1 and TL2-TB2 are close to the waist, resulting in relatively large dislocation at these locations. However, the dislocation of the longitudinal joints in the different lining rings is generally unchanged.

When the longitudinal differential settlement occurs, the dislocations of the circumferential joints become enlarged for all considered radii of the differential settlement, whereas the dislocations of the longitudinal joints remain generally unchanged. Fig. 14 shows the dislocations of the circumferential and longitudinal joints under a longitudinal differential settlement with a 300 m radius of the settlement curve. Based on the symmetry of the 11-rings model and the boundary effect in the simulation, dislocations of the joint from rings 5 to 10 were selected for analysis. It can be observed from Figs. 14(a) and 14(b) that the dislocation of the circumference joint between rings 5 and 6 is a butterfly-shaped curve, whereas the maximum values occur around the longitudinal joints (i.e., TL1-TB1, TD-TB1, TD-TB2, and TB2-TL2). However, the distribution of the dislocation in the circumferential joint between rings 9 and 10 is in the form of two attached circles, and the maximum dislocation occurs at the top and bottom of the circumferential joint.

The different distributions of dislocations in the circumferential joint can be explained by the fact that both differential settlement and differential cross-sectional deformation between two adjacent segmental rings can contribute to the dislocation of the circumferential joint. For a large differential settlement (such as that assigned to rings 9 and 10 in this simulation), the key factor affecting the dislocation is the differential settlement, whereas the differential cross-sectional deformation plays a more important role in the small differential settlement cases.

As shown in Figs. 14(c) and 14(d), there is a little difference between the dislocation values of each longitudinal joint in ring 5, whereas the dislocations of TL1-TF and TL2-TF are much larger than those of the other longitudinal joints in ring 9. However, the maximum dislocation of the longitudinal joint is less than 0.05 mm. Both dislocations of the circumferential and longitudinal joints were much larger than those solely subjected to soil pressure.

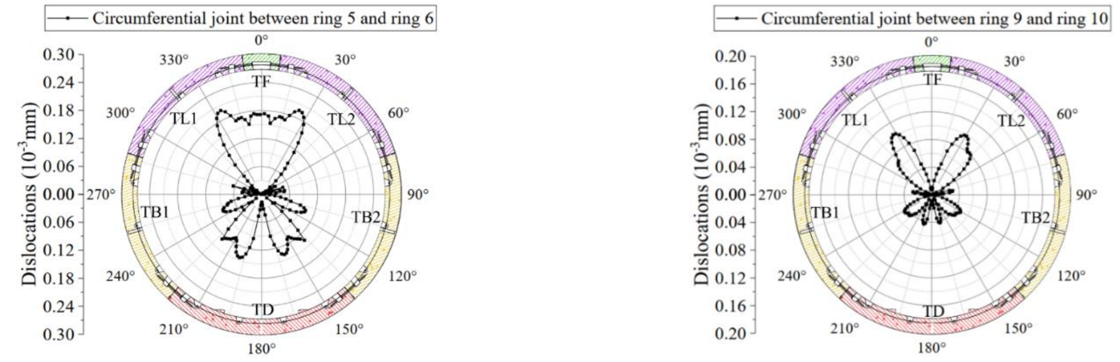

(a) Dislocations of the circumferential joint between ring 5 and ring 6

(b) Dislocations of the circumferential joint between ring 9 and ring 10

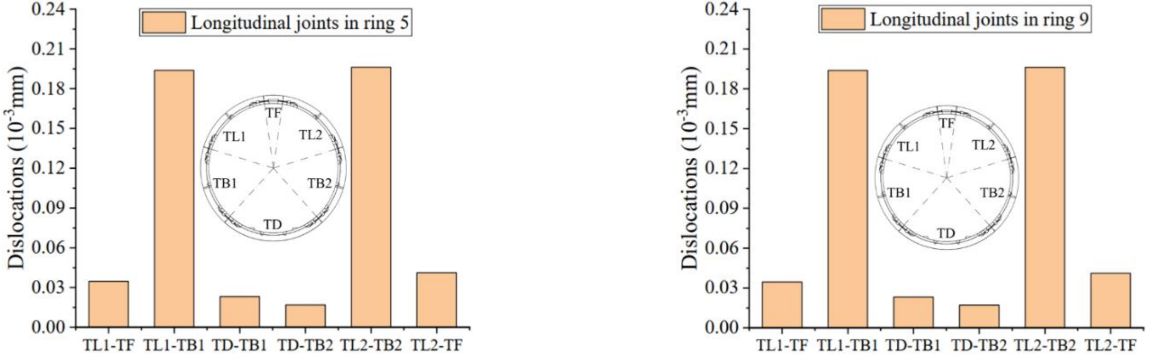

(c) Dislocations of the longitudinal joints in ring 5

(d) Dislocations of the longitudinal joints in ring 9

Fig. 13 Dislocations of the tunnel solely subjected to the soil load

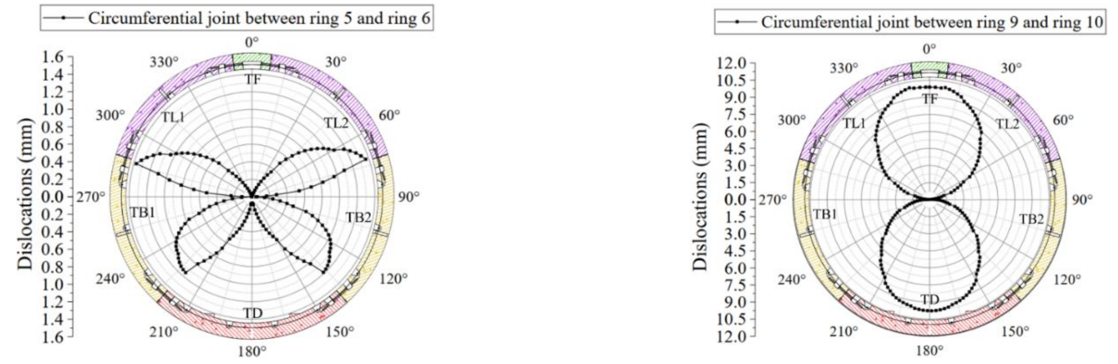

(a) Dislocations of the circumferential joint between ring 5 and ring 6

(b) Dislocations of the circumferential joint between ring 9 and ring 10

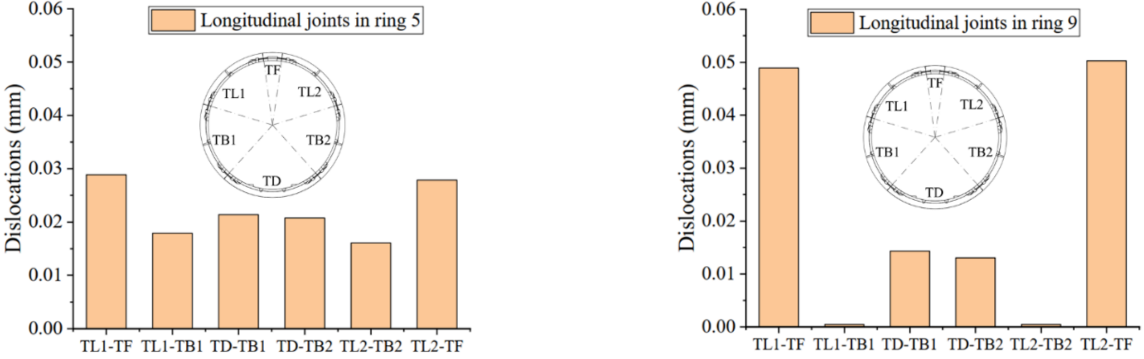

(c) Dislocations of the longitudinal joints in ring 5

(d) Dislocations of the longitudinal joints in ring 9

Fig. 14 Dislocations of the tunnel under a differential settlement with a curvature radius of 300 m

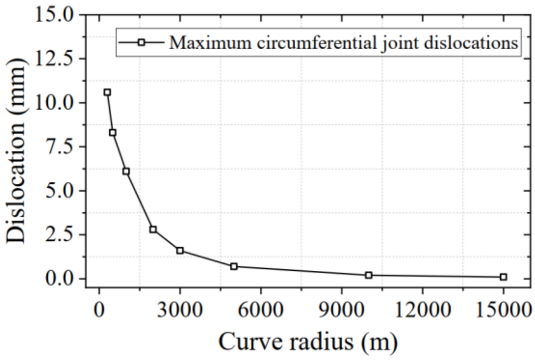

Fig. 15 Relationship between the longitudinal differential settlement curve radius and the maximum dislocation of the circumferential joint

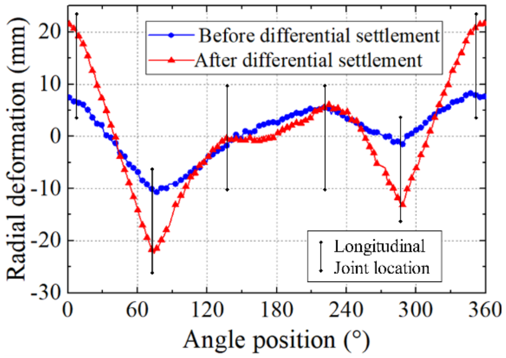

(a) Radial deformation

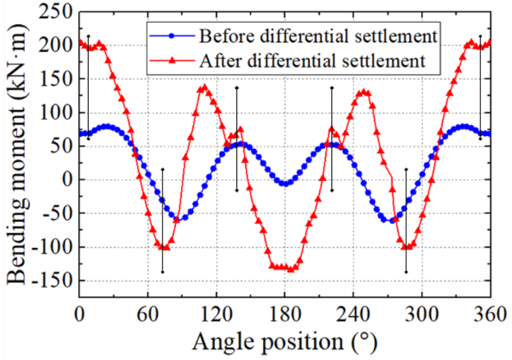

(b) Bending moment

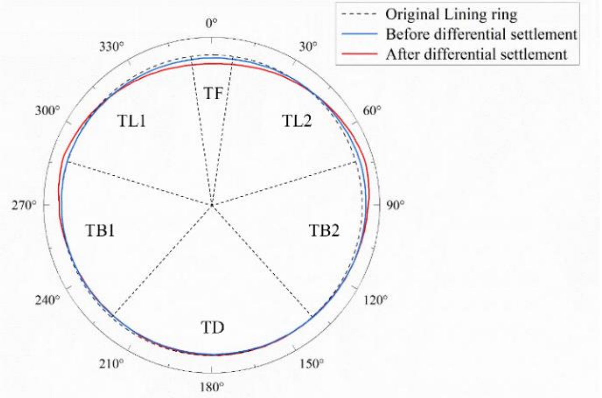

(c) Lining ring radial deformation

Fig. 16 Bending moment and radial deformation of ring 1 before and after applying the longitudinal differential settlement

The relationship between the longitudinal differential settlement curvature radius and maximum dislocation of the circumferential joint is shown in Fig. 15. It can be observed that the dislocation of the circumferential joint increases rapidly when the differential settlement curve radius is less than 1000 m. Maximum dislocation of the circumferential joint is approximately 10.6 mm when the differential settlement curve radius reaches 300 m. Because the waterproof capacity of gaskets is closely related to joint dislocations, more attention should be focused on the top and bottom of the circumferential joints where the maximum dislocation occurs.

The bending moment and radial deformation of ring 1 before and after applying the longitudinal differential settlement with a curvature radius of 300 m are shown in Fig. 16. It can be observed that the longitudinal differential settlement induces an increase in the bending moment as well as the deformation of the tunnel ring. It should be noted that when the curvature radius of the longitudinal differential settlement is 300 m, the additional bending moment at the top of the tunnel ring can be at most 1.9 times the initial one, and the additional radial deformation can be at most twice that of the initial condition, which will probably affect the safety of the tunnel structure.

4.2 Effect of the concavo-convex tenon on the dislocation

The concavo-convex tenon can contribute to improving the integrity and rigidity of the joint, thereby optimizing the bearing performance of the tunnel structure. To study its effect on the control of circumferential joint dislocations of the tunnel, the shear stiffness of the circumferential joints in the 11-ring model was updated based on the configuration of the joint with the concavo-convex tenon, which is commonly used in Shanghai Metro lines, as shown in Fig. 17. The other parameters and boundary conditions of the model remained unchanged.

Using the 3D FE model (see Fig. 18), the shear stiffness values of the circumferential joint with and without the concavo-convex tenon were obtained, and the function curves are shown in Fig. 19. It should be noted that positive axial deformation in the figure indicates that adjacent elements are compressed. The figure illustrates that the shear force increases with the axial deformation, and the shear force-dislocation curve of the joint with the concavo-convex tenon can be divided into three stages with different characteristics.

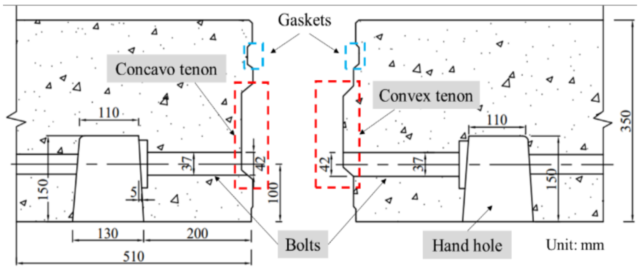

Fig. 17 Sketch of joints with the concavo-convex tenon and bolts

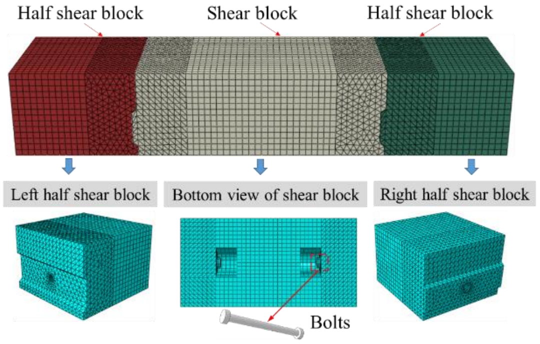

Fig. 18 Three-dimensional model for obtaining the shear stiffness joint with concavo-convex tenon

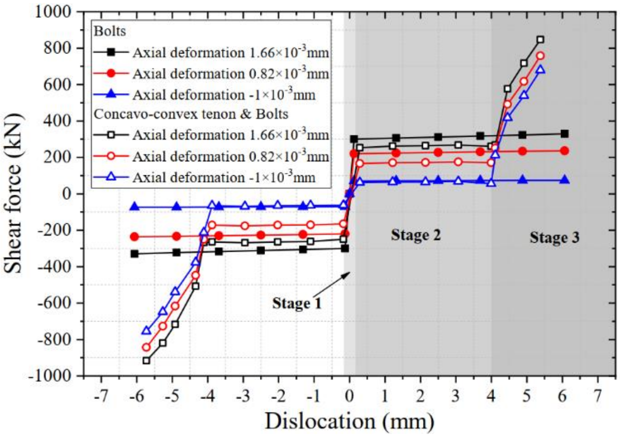

Fig. 19 Shear stiffness of the link element based on the concavo-convex tenon

In Stage 1, the shear force is less than the static friction of the joint surface, and the increase in the dislocation is relatively small. In stage 2, the dislocation increases rapidly with the shear force until it reaches 4 mm, which is the width of the void designed between the concave and convex tenons. The gap between the bolt and bolt holes also decreases in this stage. In stage 3, the shear stiffness of the joint increases rapidly as the side walls of the concave and convex tenons as well as the bolt with the bolt hole start to contact.

By applying the joint shear stiffness to the 11-ring model, the corresponding dislocations under longitudinal differential settlement could be obtained, as shown in Fig. 20. It can be concluded through a comparison of Fig. 14 and Fig. 20 that the distribution forms of the circumferential and longitudinal joint dislocations vary slightly with and without the concavo-convex tenons. However, the maximum value of the circumferential joint dislocations for the condition with the concavo-convex tenon is 4.5 mm, at the circumferential joint between ring 9 and ring 10, which is only 42% of the one without the concavo-convex tenon. The maximum longitudinal joint dislocation in the 11-ring model decreases from 0.05 mm to 0.02 mm, with concavo-convex tenon applied to the joints.

Therefore, the use of concavo-convex tenons in circumferential and longitudinal joints of the tunnel can effectively reduce the dislocations, thereby improving the waterproof capacity of the tunnel in the operation stage, especially when longitudinal differential settlement occurs.

5. Conclusions

A modified shell-joint model is proposed in this study, based on the nonlinear shear stiffness of the joint, which is a function of the axial force and dislocation value. The proposed model was verified and subsequently adopted to study the joint dislocation behaviors of a shield tunnel in Shanghai under the longitudinal differential settlement, and the following conclusions were drawn:

- A 3D FE model was employed to simulate the shear process of a longitudinal joint with bolts, which exhibited three distinct stages. During the first two stages, the bolts did not experience stress concentration. However, when the relative displacement between adjacent specimens reached 5 mm, stress concentration began to occur in the bolts.
- When the tunnel is solely subjected to the soil load, the dislocation that occurs in the longitudinal and circumferential joints is quite small, with values less than 1×10-3 mm. The maximum circumferential dislocation appears at 335° and 25°, which is around the position of the longitudinal bolt in the adjacent segment.
- Differential settlement and cross-sectional deformation can contribute to the dislocation of the circumferential joint. Circumferential joint dislocations increased rapidly when the differential settlement curvature radius was less than 1000 m. When the curvature radius of the longitudinal differential settlement reached 300 m, the maximum circumferential joint dislocation in the 11-ring model was 10.3 mm, which might lead to leakage and even waterproof failure of the tunnel structure.

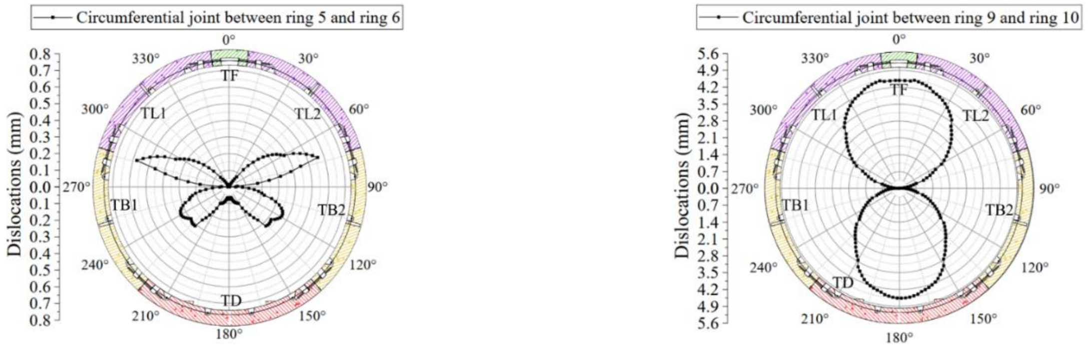

(a) Dislocations of the circumferential joint between ring 5 and ring 6

(b) Dislocations of the circumferential joint between ring 9 and ring 10

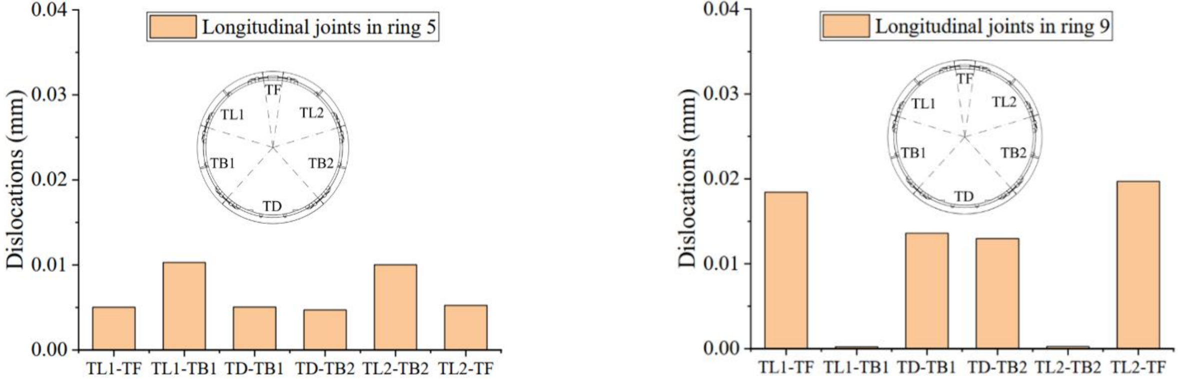

(c) Dislocations of the longitudinal joints in ring 5

(d) Dislocations of the longitudinal joints in ring 9

Fig. 20 Dislocations of the tunnel with concavo-convex tenons under a differential settlement with a curvature radius of 300 m

- With concavo-convex tenon applied to the longitudinal and circumferential joints, the difference of different joint dislocation of the same segment ring is reduced. The maximum circumferential joint dislocation decreased from 10.3 mm to 4.5 mm and the maximum longitudinal joint dislocation decreased from 0.05 mm to 0.02 mm, which will improve the waterproof capacity of the tunnel in the operation stage.

Acknowledgments

This research was funded by the National Natural Science Foundation of China grant number 52208443, Natural Science Foundation of Shanghai grant number 22ZR1466500, and China Postdoctoral Science Foundation grant number 2022M722958.

References

Chen, R.P., Meng, F.Y., Ye, Y.H. and Liu, Y. (2018), “Numerical simulation of the uplift behavior of shield tunnel during the construction stage”, *Soils Found.*, **58**(2), 370-381. https://doi.org/10.1016/j.sandf.2018.02.007.

Chen, Z.J., Yang, Z.H. and Li, D.M. (2010), “Study on mechanical properties of longitudinal joint of segmental lining of Shanghai Yangtze River Tunnel”, *Tunnel Rail Transit*, (04), 17-19+63 (in Chinese). https://doi.org/10.13547/j.cnki.dxgcysd.2010.04.011.

Ding, W.Q., Gong, Y.F., Qiao, Y.F. and Gong, C.J. (2020), “Experimental investigation on the mechanical behavior of segmental joint under combined loading of compression-bending-shear”, *Tunn. Undergr. Sp. Tech.*, **98**. doi:10.1016/j.tust.2020.103346

Do, N.A., Dias, D., Oreste, P. and Djeran-Maigre, I. (2014) “2D numerical investigations of twin tunnel interaction”, *Geomech. Eng.*, **6**(3), 263–275. https://doi.org/10.12989/gae.2014.6.3.263.

Eskandari, F., Goharrizi, K.G. and Hooti, A. (2018), “The impact of EPB pressure on surface settlement and face displacement in intersection of triple tunnels at Mashhad metro”, *Geomech. Eng.*, **15**(2), 769-774. https://doi.org/10.12989/gae.2018.15.2.769.

Feng, K., He, C., Qiu, Y., Zhang, L., Wang, W., Xie, H.M., Zhang, Y.Y. and Cao, S.Y. (2018), “Full-scale tests on bending behavior of segmental joints for large underwater shield tunnels”, *Tunn. Undergr. Sp. Tech.*, **75**, 100-116. https://doi.org/10.1016/j.tust.2018.02.008.

GB 50010-2010(2010), Code for Design of Concrete Structures, National Standard of the People's Republic of China; Beijing, China

Gong, W.P., Juang, C.H., Huang, H.W., Zhang, J. and Luo, Z. (2015), “Improved analytical model for circumferential behavior of jointed shield tunnels considering the longitudinal differential settlement”, *Tunn. Undergr. Sp. Tech.*, **45**, 153-165. https://doi.org/10.1016/j.tust.2014.10.003.

Hasan, M. and Abdullah, N.M. (2019), “Deformation and crack analysis of tunnel structure subjected to static distributed load using Pseudoshell model”, *IOP Conference Series: Materials Science and Engineering*, **523**, 012034. https://doi.org/10.1088/1757-899X/523/1/012034

Jin, Y.L., Ding, W.Q., Yan, Z.G., Soga, K. and Li, Z.L. (2017), "Experimental investigation of the nonlinear behavior of segmental joints in a water-conveyance tunnel", *Tunn. Undergr. Sp. Tech.*, **68**, 153-166. https://doi.org/10.1016/j.tust.2017.05.018.

Kim, N.Y., Park, D.H., Jung, H.S. and Kim, M. I. (2020), "Deformation characteristics of the tunnel bottom after construction under geological conditions of long-term deformation", *Geomech. Eng.*, **21**(2), 171-178. https://doi.org/10.12989/gae.2020.21.2.171

Lei, M.F., Lin, D.Y., Shi, C.H., Ma, J.J. and Yang, W.C. (2018), "A structural calculation model of shield tunnel segment: heterogeneous equivalent beam model", *Adv. Civil Eng.*, 2018. https://doi.org/10.1155/2018/9637838.

Li, B.Q., Zhang, Z.Y., Wang, X.G. and Liu, X.N. (2019), "Investigation on cohesive zone model of bolted joint for water conveyance tunnel lining", *Eng. Comput.*, **36**(5), 1449-1468. https://doi.org/10.1108/ec-07-2018-0310.

Li, D.M., Chen, Z.J. and Yang, Z.H. (2011), "Test and analysis of shear performance of circumferential joint of the segment ring in Shanghai Yangtze River Tunnel", *Tunnel. Rail Transit.*, (01), 15-17+52 (in Chinese). https://doi.org/10.13547/j.cnki.dxgcysd.2011.01.007.

Li, Z., Soga, K., Wang, F., Wright, P. and Tsuno, K. (2014), "Behavior of cast-iron tunnel segmental joint from the 3D FE analyses and development of a new bolt-spring model", *Tunn. Undergr. Sp. Tech.*, **41**, 176-192. https://doi.org/10.1016/j.tust.2013.12.012.

Liu, X., Zhang, W. and Wang, D. (2016), "Experimental study on shear performance of longitudinal joint in quasi-rectangular shield tunnel", *J. Rail Way Sci. Eng.*, **13**(9), 1767-1775.

Nawel, B. and Salah, M. (2015), "Numerical modeling of two parallel tunnels interaction using three-dimensional finite elements method", *Geomech. Eng.*, **9**(6), 775-791. https://doi.org/10.12989/gae.2015.9.6.775.

Nikadat, N. and Marji, M.F. (2016), "Analysis of stress distribution around tunnels by hybridized FSM and DDM considering the influences of joints parameters", *Geomech. Eng.*, **11**(2), 269-288. https://doi.org/10.12989/gae.2016.11.2.269.

Salemi, A., Esmaeili, M. and Sereshki, F. (2015), "Normal and shear resistance of longitudinal contact surfaces of segmental tunnel linings", *Int. J. Rock Mech. Min. Sci.*, **77**, 328-338. https://doi.org/10.1016/j.ijrmms.2015.04.014.

Shi, C.H., Cao, C.Y., Lei, M.F. and Yang, W.C. (2019), "Sealant Performance Test and Stress-Seepage Coupling Model for Tunnel Segment Joints", *Arabian J. Sci. Eng.*, **44**(5), 4201-4212. https://doi.org/10.1007/s13369-018-3357-1

Shi, C.H., Cao, C.Y., Lei, M.F., Peng, L.M. and Ai, H.J. (2016), "Effects of lateral unloading on the mechanical and deformation performance of shield tunnel segment joints", *Tunn. Undergr. Sp. Tech.*, **51**, 175-188. https://doi.org/10.1016/j.tust.2015.10.033

Talmon, A.M. and Bezuijen, A. (2013), "Analytical model for the beam action of a tunnel lining during construction", *Int. J. Numer. Anal. Method. Geomech.*, **37**(2), 181-200. https://doi.org/10.1002/nag.1092.

Tvede-Jensen, B., Faurschou, M. and Kasper, T. (2017), "A modeling approach for joint rotations of segmental concrete tunnel linings", *Tunn. Undergr. Sp. Tech.*, **67**, 61-67. https://doi.org/10.1016/j.tust.2017.04.019.

Wang, B. (2007), "Analysis and test for lining the whole wreath of Shanghai—Chongming tunnel", Master Dissertation; Tongji University, Shanghai, China (in Chinese).

Wang, J.C., Huang, W.M., Xu, R.Q., Yang, Z.X. and Xu, R.Q. (2020), "Analytical approach for circular-jointed shield tunnel lining based on the state space method", *Int. J. Numer. Anal. Method. Geomech.*, **44**(5), 575-595. https://doi.org/10.1002/nag.3012.

Wang, M.N., Dong, Y.C., Yu, L., Fang, L., Wang, X.L. and Liu, D.G. (2019), "Experimental and numerical researches of precast segment under radial dislocation conditions", *Tunn. Undergr. Sp. Tech.*, **92**. https://doi.org/10.1016/j.tust.2019.103055.

Wang, Z., Wong, R.C.K. and Heinz, H. (2010), "Assessment of long-term behavior of a shallow tunnel in clay till", *Geomech. Eng.*, **2**(2), 107-123. https://doi.org/10.12989/gae.2010.2.2.107.

Wu, H.N., Shen, S.L., Liao, S.M. and Yin, Z.Y. (2015), "Longitudinal structural modeling of shield tunnels considering shearing dislocation between segmental rings", *Tunn. Undergr. Sp. Tech.*, **50**, 317-323. https://doi.org/10.1016/j.tust.2015.08.001.

Wu, H.N., Shen, S.L., Yang, J. and Zhou, A.N. (2018), "Soil-tunnel interaction modeling for shield tunnels considering shearing dislocation in longitudinal joints", *Tunn. Undergr. Sp. Tech.*, **78**, 168-177. https://doi.org/10.1016/j.tust.2018.04.009.

Yan, Q.X., Zhang, C.A., Wu, W., Zhu, H.X. and Yang, W.B. (2019), "3D numerical simulation of shield tunnel subjected to swelling effect considering the nonlinearity of joint bending stiffness", *Periodica Polytechnica-Civil Engineering*, **63**(3), 751-762. https://doi.org/10.3311/PPci.13996.

Yang, F., Cao, S. R., and Li, Q. B. (2019), "An analytical model for the rotational behavior of concrete segmental joints with gaskets", *Adv. Struct. Eng.*, **22**(13), 2866-2881. https://doi.org/10.1177/1369433219852566.

Yoo, C., and Cui, S. (2020), "Effect of new tunnel construction on the structural performance of existing tunnel lining", *Geomechanics and Engineering*, **22**(6), 497–507. https://doi.org/10.12989/gae.2020.22.6.497

Zaid, M. (2021), "Three dimensional finite element analysis of urban rock tunnel under static loading condition: Effect of the rock weathering", *Geomech. Eng.*, **25**(2), 99-109. https://doi.org/10.12989/gae.2021.25.2.099.

Zhang, D.M., Liu, Z.S., Wang, R.L. and Zhang, D.M. (2019a), "Influence of grouting on rehabilitation of an over-deformed operating shield tunnel lining in soft clay", *Acta Geotechnica*, **14**(4), 1227-1247. https://doi.org/10.1007/s11440-018-0696-8

Zhang, L., Feng, K., Li, M.R., Sun, Y.P., He, C. and Xiao, M.Q. (2019b), "Analytical method regarding the compression-bending capacity of segmental joints: Theoretical model and verification", *Tunn. Undergr. Sp. Tech.*, **93**. https://doi.org/10.1016/j.tust.2019.103083.

Zhang, X., Lin, Z., Zhang, K., Di, H., He, C. and Zhou, S. (2023a), "Full–scale experimental test for load–bearing behavior of the carbon fiber shell reinforced stagger–jointed shield tunnel", *Compos. Struct.*, **311**, 116773. https://doi.org/10.1016/j.compstruct.2023.116773.

Zhang, X., Zhou, S. and Di, H. (2023b), "Semi–analytical solution for ultimate bearing capacity of straight–jointed segmental tunnel lining", *Tunn. Undergr. Sp. Tech.*, **138**, 105160. https://doi.org/10.1016/j.tust.2023.105160.

Zhang, Z.X., Zhang, J.Q., Huang, X. and Zhuang, Q.W. (2020), "Experimental study on prediction of long-term durability of sealing gasket of shield tunnel", *J. Zhejiang Univ.*, (Engineering Science), **54**(1), 118-125(in Chinese).

Zhao, W.S., Chen, W.Z. and Yang, F. (2015), "Study of the interface mechanical properties of concrete segments in shield tunnels", *Modern Tunn. Tech.*, **52**(3), 119-126. https://doi.org/10.13807/j.cnki.mtt.2015.03.017.

Zou, J.F., Chen, K.F. and Pan, Q.J. (2017), "Influences of seepage force and out-of-plane stress on cavity contracting and tunnel opening", *Geomech. Eng.*, **13**(6), 907-928. https://doi.org/10.12989/gae.2017.13.6.907.

Zuo, L.B., Li, G.H., Feng, K., Ma, X.C., Zhang, L., Qiu, Y., Cao, S.Y. and Feng, L. (2018), "Experimental analysis of mechanical behavior of segmental joint for gas pipeline shield tunnel under unfavorable compression-bending loads”, *Tunn. Undergr. Sp. Tech.*, **77**, 227-236. https://doi.org/10.1016/j.tust.2018.03.005.

CC